physica status solidi (RRL) – Rapid Research Letters

RESEARCH ARTICLE OPEN ACCESS

Epitaxy and Phase Stability of 2D Hexagonal Gallium Telluride on Silicon

Andrea Pianetti[1,2] | Stefano Cecchi[1,3] | Michael Hanke[1] | Jonathan J. Finley[4] | Fabrizio Arciprete[5] | Raffaella Calarco[1,6] | Eugenio Zallo[1,4]

[1]Paul-Drude-Institut für Festkörperelektronik, Leibniz-Institut im Forschungsverbund Berlin e.V., Berlin, Germany | [2]Center for Nanoscience and Technology, Istituto Italiano di Tecnologia, Milano, Italy | [3]Department of Materials Science, University of Milano-Bicocca, Milano, Italy | [4]Walter-Schottky-Institut and TUM School of Natural Sciences, Technische Universität München, Garching, Germany | [5]Dipartimento di Fisica, Università di Roma "Tor Vergata", Rome, Italy | [6]Institute for Microelectronics and Microsystems (IMM), Consiglio Nazionale delle Ricerche (CNR), Rome, Italy

Correspondence: Eugenio Zallo (eugenio.zallo@tum.de)

Received: 24 October 2025 | **Revised:** 27 November 2025 | **Accepted:** 1 December 2025

Keywords: 2D materials | amorphization | gallium telluride | phase transformation | van der Waals epitaxy

ABSTRACT

Controlling crystal quality during epitaxial growth is essential for the advancement of novel materials with industrial relevance. Here, we investigate the molecular beam epitaxy of 2D hexagonal gallium telluride (h-GaTe) on silicon, focusing on the roles of substrate temperature, flux ratio, and surface treatment. Real-time monitoring through line-of-sight quadrupole mass spectrometry and reflection high-energy electron diffraction reveals a transition from 2D to 3D growth after the deposition of a critical number of layers, a process not attributable to strain relaxation. Structural and optical characterization by atomic force microscopy, X-ray diffraction, Raman spectroscopy, and photoluminescence confirm the formation of large-area, high-crystalline-quality h-GaTe via van der Waals epitaxy. The thermal stability of h-GaTe was further assessed through systematic annealing, which revealed that the as-grown hexagonal phase undergoes amorphization followed by a transformation into an optically active, ordered phase at higher temperatures. These findings highlight the pathways to engineer 2D GaTe layers with controlled structure and properties, offering insights into their integration in next-generation optoelectronic devices.

1 | Introduction

Gallium telluride (GaTe) is part of the family of post-transition metal monochalcogenides (PTMCs) with the general formula $M_{III}X$ (M_{III} = Ga, In, Al; X = S, Se, Te). Unlike transition metal dichalcogenides, these compounds contain lighter group-III cations, which result in softer lattices, unusual vibrational behavior, and pronounced anharmonicity [1, 2]. Such characteristics underpin their strong nonlinear optical responses and make them attractive for optoelectronic applications. In its stable monoclinic form (m-GaTe), the material is a direct-bandgap semiconductor with demonstrated applications in radiation detection [3], visible-light photodetectors [4, 5], and broadband absorption [6]. By contrast, the metastable hexagonal polymorph (h-GaTe) exhibits a quasidirect gap in the multilayer regime, making it promising for thermoelectric energy conversion [7], while theoretical studies predict half-metallicity in the few-layer limit [8]. Despite these prospects, only limited attempts at thin film synthesis of h-GaTe have been reported [9], reflecting the difficulty of stabilizing this phase. Furthermore, surface reactivity [10] makes the understanding of the pristine information from telluride materials even more challenging. Molecular beam epitaxy (MBE) provides precise control over growth parameters and enables insitu monitoring, making it a powerful approach for the synthesis of PTMCs [11–15]. Recently, our group demonstrated the large-area van der Waals (vdW) epitaxy of h-GaTe on Sb-passivated Si(111), with subsequent transformation to m-GaTe upon annealing [16]. Complementary studies by Quan et al. [17] revealed phase modulation in GaTe driven by strain and

This is an open access article under the terms of the Creative Commons Attribution License, which permits use, distribution and reproduction in any medium, provided the original work is properly cited.

© 2025 The Author(s). *physica status solidi (RRL) Rapid Research Letters* published by Wiley-VCH GmbH.

thickness, while vdW epitaxy of h-GaTe on graphene/SiC provided insight into growth kinetics [18]. Yet, the influence of growth parameters on lattice relaxation during h-GaTe epitaxy on conventional semiconductors remains unexplored. Moreover, the mechanism of phase transformation into the optically active structure is still unclear, despite its critical importance for device integration. In this work, we investigate the epitaxial growth of multilayer h-GaTe on Si(111) by systematically varying substrate temperature (T_{sub}), Ga/Te flux ratio ($\Phi_{Ga/Te}$), and in the presence of surface passivation. Using insitu characterization tools such as reflection high-energy electron diffraction (RHEED) and quadrupole mass spectrometry (QMS), we disentangle the respective roles of Ga and Te, demonstrating that Ga flux dominates the kinetics of vdW epitaxy, enabling the synthesis of large-area h-GaTe with high-crystalline quality. The evolution of the in-plane lattice spacing with growth time reveals differences in the interfacial region; however, it converges to comparable structural characteristics as growth proceeds, accompanied by reduced mass transport across layers and enhanced island formation. Post-growth X-ray diffraction (XRD), Raman spectroscopy, and photoluminescence (PL) measurements as a function of annealing temperature show that the as-grown h-GaTe undergoes a three-step transformation: two amorphous phases, followed by the emergence of an optically active crystalline phase at higher temperatures. Finally, the effectiveness and thermal robustness of ZnS-SiO_2 as a capping layer are assessed. Overall, this work provides new insights into the phase stability and transformation of metastable h-GaTe, advancing its integration as a PTMC platform on silicon.

2 | Results and Discussion

The first section addresses the influence of growth parameters on the epitaxy of h-GaTe on Si(111). Variations in T_{sub}, $\Phi_{Ga/Te}$, and initial surface preparation are correlated with changes in growth dynamics, lattice relaxation, morphology, and growth rate. Section 2.2 focuses on the thermal stability of h-GaTe, where annealing experiments reveal the evolution of the hexagonal phase and the response of the capping layer.

2.1 | Epitaxial Growth

Four epitaxial samples were realized by individually tuning T_{sub}, $\Phi_{Ga/Te}$, and substrate passivation (A–D, see Table 1). Due to the high reactivity of the GaTe surface in the ambient environment, the films were capped by sputtering in the load lock with ≈30 nm thick ZnS-SiO_2 amorphous layers after sample cooling to room temperature (RT) and before taking it out of the MBE chamber. All experiments were carried out on 2×2 cm^2 Si(111) substrates that were chemically cleaned [19] and reconstructed to the 7 × 7 at 750°C (see Experimental Section). A lower T_{sub} limit of ≈350°C was identified, below which crystalline GaTe does not form, while an upper limit near 400°C favors the growth of atomically smooth crystalline GaTe over the amorphous phase. However, complete Te desorption at 400°C (sticking coefficient ≈0) [20] sets an upper boundary for a reasonable GaTe growth rate, and low $\Phi_{Ga/Te}$ ($1/75 - 1/50$) was required. This matches the finding from Ref. [11] where the importance of a large chalcogen flux for PTMC GaSe was emphasized. The critical role of the Ga flux and the $\Phi_{Ga/Te}$ in controlling the growth rate of h-GaTe on Sb-passivated Si(111) was previously reported by our group [16]. The confirmation of the GaTe growth in the hexagonal phase for all samples was obtained by XRD and Raman (see Section 2.2).

2.1.1 | Effect of Substrate Temperature

The first growth experiment (sample A) was performed at a substrate temperature of 390°C, close to the upper limit of 400°C, with $\Phi_{Ga/Te}$ of ≈1/70. The analysis of the RHEED pattern during growth allowed us to track the evolution of the in-plane lattice spacing and study the strain relaxation process, as shown in Figure 1a. The distance between RHEED streaks in reciprocal space was calibrated using the Si(111)-(7 × 7) surface as a reference (lattice parameter of 3.84 Å). During the first 10 min of growth, a transition from the Si pattern to the epilayer pattern is observed through a blurred intermediate phase (not shown). The lattice parameter rapidly increases, reaching a plateau value of 4.111 ± 0.001 Å after the completion of the bilayer (BL, see the green dotted line in Figure 1a), close to the final value at the end of the growth of 4.117 ± 0.001 Å (see the blue dotted line in Figure 1a), which is about 1.4% larger than the literature value of 4.06 Å [9]. The small further increase detected after BL formation is likely due to changes in thermal conductivity, heat absorption, and kinetic roughening as the film thickens (see the decrease in RHEED oscillations in Figure S1, Supporting Information). The mismatch between the substrate and h-GaTe is estimated to be around 5.1%. However, since the 2D to 3D transition occurs only after the lattice is fully relaxed (see Figure S1, Supporting Information), it cannot be attributed

TABLE 1 | Summary of the main properties of the epitaxial samples A–D. The table reports the substrate temperature (T_{sub}), GaTe flux ratio ($\Phi_{Ga/Te}$), the in-plane lattice spacing (a) obtained from the streaks separation at the end of the growth in the reflection high-energy electron diffraction (RHEED) pattern, the relaxation time of the RHEED signal after the first plateau, the film thickness (average value of X-ray reflectivity, X-ray diffraction-XRD fringes and RHEED oscillations, see more details in Table S1, Supporting Information), the nominal growth rate (thickness/growth time), and the surface roughness from atomic force microscopy (AFM) topography. The growth time is 80 min for all the samples.

Samples	T_{sub}, °C	$\Phi_{Ga/Te}$	Sub. passivation	a, Å	Relax. time, min	Thickness, nm	Nominal g. r., nm min^{-1}	Roughness, nm
A	390	1/70	No	4.117 ± 0.001	20	8.3 ± 0.2	0.107	0.440 ± 0.001
B	375	1/74	No	4.118 ± 0.001	15	8.8 ± 0.2	0.110	0.490 ± 0.001
C	375	1/72	Yes	4.120 ± 0.001	10	9.7 ± 0.2	0.121	0.460 ± 0.001
D	375	1/48	Yes	4.093 ± 0.001	7	15.1 ± 0.4	0.189	0.860 ± 0.001

18626270, 2026, 2, Downloaded from https://onlinelibrary.wiley.com/doi/10.1002/pssr.202500432 by CochraneItalia, Wiley Online Library on [12/06/2026]. See the Terms and Conditions (https://onlinelibrary.wiley.com/terms-and-conditions) on Wiley Online Library for rules of use; OA articles are governed by the applicable Creative Commons License

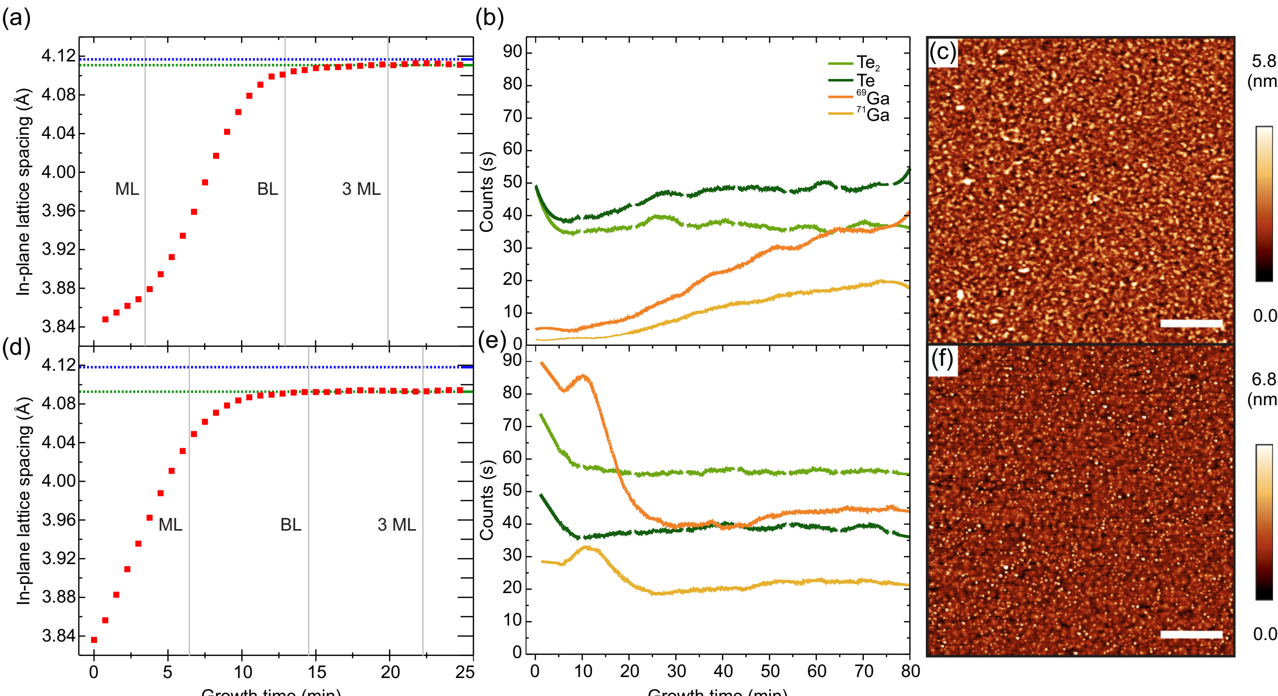

FIGURE 1 | Effect of substrate temperature. (a and d) In-plane lattice spacing evolution as a function of time during the first 25 min of the MBE growth for samples A and B, respectively. The lattice parameter is calculated from the streak distance in the in situ RHEED patterns acquired perpendicular to the Si < 1–10 > direction. The layer thickness dependency (monolayer-ML, bilayer-BL, ...) is obtained from the specular spot RHEED oscillations (see Figure S1, Supporting Information). The green and blue dotted lines represent the first plateau and the final growth time, respectively. (b and e) Quadrupole mass spectrometry signal recorded during the entire growth process for samples A and B, respectively, showing the evolution of different Ga- and Te-containing species. Periodic interruptions in Te and Te_2 intensities correspond to the use of a shutter, which is required due to their high chemical reactivity. (c and f) AFM height image of the h-GaTe at the end of the growth of samples A and B, respectively, after the deposition of the capping layer before taking them out of the MBE chamber. Scale bar in (c,f) is 1 μm.

to strain relaxation. Instead, consistent with vdW epitaxy, the transition is governed by surface kinetics: as homoepitaxial growth progresses, the low surface energy of the atoms in this regime increases the barrier for lateral diffusion and interlayer mass transport, promoting the formation of 3D islands, as observed in Ref. [18]. QMS analysis (see Figure 1b and Experimental Section for details) reveals that the Te_2 signal, after an initial drop, oscillates around a constant value, while Te exhibits a slow monotonic increase. Ga isotopes (69 and 71) show steady incorporation for the first 10 min, followed by a progressive increase with a stepped profile. The combination of an almost constant Te signal and gradually increasing Ga desorption indicates that the growth occurs under Ga-rich conditions. Excess Ga accumulates on the surface and desorbs, allowing the system to maintain near-stoichiometric GaTe layers. Atomic force microscopy (AFM) measurements (see Figure 1c and Table 1) exhibit a predominantly flat surface but covered by numerous nanometric islands (diameter: 45–90 nm, height: 1.5–2 nm). The formation of 3D features is consistent with the slightly spotty RHEED pattern observed after 35 min (not shown). The observed triangular features (side length of ≈75 ± 5 nm) likely correspond to individual twin domains rotated by 60°. Based on the thickness determined by the average of XRD Laue thickness oscillations, X-ray reflectivity (XRR) and RHEED oscillations, we calculate a nominal growth rate of 0.107 nm min^{-1} (see Table 1 and Supporting Information).

The effect of temperature was evaluated by conducting a second growth at 375°C, while keeping all other parameters unchanged (sample B). As reported in Figure 1d, the lattice parameter evolution shows a faster relaxation, with the steady value of 4.093 ± 0.001 Å reached during the formation of the BL. Afterward, it oscillates during the third layer formation, followed by a monotonic increase until the end of growth, with a final value of 4.118 Å, which is comparable to that of sample A. QMS data (Figure 1e) indicate a constant Te_2 signal after the initial drop, while Te stabilizes at a constant value, demonstrating higher Te incorporation than the growth at lower temperature, even though the element is still in excess. An unusual initial Ga peak is detected, followed by a drop to a steady value after 20 min, missing the steady increase observed in Figure 1b. We tentatively attribute the large Ga signal to some transient instability of the Ga cell or the presence of Ga clusters on the sample block. By considering only the second part of the measurement (after 20 min), we can infer that the incorporation of both species increases with lower temperature, as expected from the larger sticking coefficient. AFM data (see Figure 1f and Table 1) show slightly higher roughness and higher density of bright spots than sample A. The islands have diameters of 50–70 nm and heights of 2–3 nm, while triangular features appear clearer and slightly larger (side length ≈100 ± 5 nm). This result aligns with the RHEED data, where the spotty pattern emerges after only 20 min (see Figure S1, Supporting Information). The nominal

18626270, 2026, 2, Downloaded from https://onlinelibrary.wiley.com/doi/10.1002/pssr.202500432 by CochraneItalia, Wiley Online Library on [12/06/2026]. See the Terms and Conditions (https://onlinelibrary.wiley.com/terms-and-conditions) on Wiley Online Library for rules of use; OA articles are governed by the applicable Creative Commons License

growth rate of 0.110 nm min^{-1} confirms that lower substrate temperature increases incorporation.

2.1.2 | Effect of Substrate Passivation

GaTe growth was realized on Sb-passivated Si(111) substrates (see Experimental Section). Sb saturates the Si dangling bonds, preventing Ga and Te from bonding directly with the substrate and favoring vdW epitaxy [16]. As shown in Figures 1d–f and 2a–c, we compare the case without and with substrate passivation, respectively, where T_{sub} and $\Phi_{Ga/Te}$ are kept the same (see samples B and C, respectively, in Table 1). RHEED observations reveal a different early-stage dynamic compared to non-passivated growth, with an intermediate pattern appearing in the time interval 2–4.5 min and corresponding to an in-plane lattice spacing of 3.88 Å (see Figure 2a). These streaks arise from the Sb/Ga transition BL at the interface between the Si substrate and h-GaTe (see Figure S2, Supporting Information). As shown in Figure 2a, the lattice parameter extracted from RHEED in sample C relaxes in the second layer by reaching a plateau of 4.102 Å in 10 min. This is faster than the case of sample B (see Figure 1d), where a linear relaxation takes place during the first layer, and highlights the more effective vdW gap formation with the passivation step. After 4 monolayers (MLs), the lattice parameter slowly increases to 4.120 Å, alike the non-passivated samples (see Table 1). It is important to note that the 2D to 3D transition occurs ≈20 min after the start in both samples (see Figure S1, Supporting Information). This suggests that substrate passivation significantly affects the initial growth kinetics but becomes less relevant once the first few GaTe layers (≈3 MLs) are established. The grazing incidence diffraction (GID)-XRD analysis (see Experimental Section for details and Figure S3, Supporting Information) matches the results of in-plane spacings derived from RHEED for both samples. Furthermore, the angular dependence reveals a 60° periodicity, originating from twin domains whose formation is facilitated by the weak vdW coupling at the interface [16]. Remarkably, only sample C exhibits an additional 30° component, which highlights the stronger epitaxial registry with the substrate in the absence of the passivation treatment. QMS trend for sample C (see Figure 2b) indicates a slow increase of the different species after the first two layers and a stepped profile, similar to sample A. However, the still present desorption could explain the different growth mode, with a change in surface energy as a function of thickness. The AFM data further support the hypothesis of comparable growth in the thicker regime (see Figures 2c, 1f and Table 1) with a slightly improved crystalline quality, as shown by the reduced roughness (0.49 and 0.46 nm for samples B and C, respectively), and a larger growth rate (0.121 nm min^{-1}).

2.1.3 | Effect of Ga/Te Flux Ratio

Figure 2 reports a side-by-side comparison of the samples C and D (upper and lower panels), where h-GaTe is grown on Sb-passivated Si(111) at 375°C with $\Phi_{Ga/Te}$ of 1/70 and 1/48, respectively (see Table 1). The growth rate for sample D increases markedly, as evidenced by the larger film thickness (see Table 1). In addition, the 2D growth regime is sustained for a longer duration before 3D features emerge after ≈60 min and no RHEED oscillations are observed (not shown), as compared with the onset of the spotty diffraction for sample C (see Figure S1, Supporting Information). The undetectable intensity modulation and late-appearing spots are tentatively attributed to a two-stage effect, with an initial Ga-rich surface chemistry followed by delayed islanding. Interestingly, improved interface quality in Ge/SiGe multilayers at lower temperature (equivalent

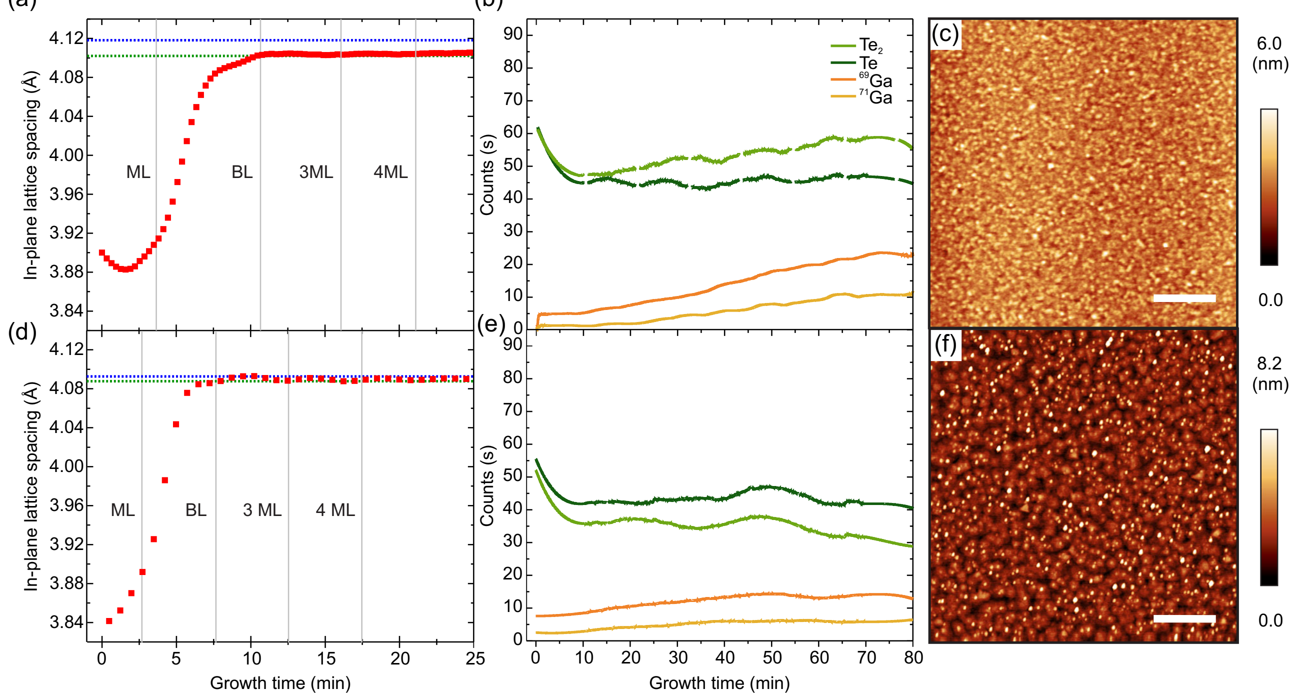

FIGURE 2 | Effect of Ga/Te flux ratio. Same description as in Figure 1 for samples (a–c) C and (d–f) D. The RHEED patterns are acquired perpendicular to the Si < 11–2 > (Si < 1–10 >) for sample C (D). Scale bar in (c,f) is 1 µm.

18626270, 2026, 2, Downloaded from https://onlinelibrary.wiley.com/doi/10.1002/pssr.202500432 by CochraneItalia, Wiley Online Library on [12/06/2026]. See the Terms and Conditions (https://onlinelibrary.wiley.com/terms-and-conditions) on Wiley Online Library for rules of use; OA articles are governed by the applicable Creative Commons License

to a higher growth rate) has been reported in Ref. [21] and attributed to the kinetic suppression of interface roughening. The in-plane lattice spacing evolution (see Figure 2d) is similar to that of sample C with faster relaxation (≈6 min). Another analogy is the lattice parameter oscillation, which occurs a couple of times at 4.088 Å before the quasi-linear increase until the end of growth, with a final value of 4.098 Å. This corresponds to a change of only 0.9% from the literature value. Two different physical mechanisms have been proposed to explain oscillations of the in-plane lattice spacing measured by RHEED during layer-by-layer growth: elastic relaxation around island edges [22] and an instrumental/kinematic effect in which the finite angular dispersion of the RHEED beam and detector averages a time-dependent island-size scattering distribution [23]. We advance that the dependence of oscillation amplitude on island density in our h-GaTe/Si(111) system, where vdW epitaxy reduces elastic coupling to the substrate, is naturally accounted for by the angular-dispersion/island-size mechanism. In fact, sample D shows a larger amplitude of parameter oscillations due to the sparser and larger islands. Nevertheless, we cannot exclude an elastic contribution a priori, and a more thorough understanding could be obtained from correlating RHEED shifts with independent strain probes (GID-XRD, Raman) and insitu AFM or scanning tunneling microscopy island statistics, which could help discriminate between the two effects. QMS traces recorded at higher $\Phi_{Ga/Te}$ (see Figure 2e) show reduced Ga desorption together with a decreasing Te signal. In contrast, sample C (Figure 2b) exhibits a continuous increase in both Ga and Te signals throughout the growth (after the initial incorporation phase). This behavior demonstrates Ga-dominated kinetics, as a decrease in the $\Phi_{Ga/Te}$ not only enhances Ga desorption but also suppresses Te incorporation. The nominal growth rate for sample D reaches 0.189 nm min^{-1}, ≈60% higher than that of sample C. Morphologically, the higher $\Phi_{Ga/Te}$ condition results in more pronounced triangular features and slightly increased roughness, which can be attributed to the greater thickness achieved under the faster growth rate (see Figure 2c,f and Table 1).

2.2 | Phase Stability

Given the metastable nature of as-grown h-GaTe, we investigate its structural evolution under thermal treatment in the following section. Two approaches were employed to probe the phase transformation process: rapid thermal annealing (RTA) [24] and insitu annealing on a hot plate. These complementary methods provide insights into the stability and transformation pathways of the hexagonal phase. Finally, PL measurements were performed on RTA samples to assess the emergence of optical activity in the transformed material.

2.2.1 | RTA

RTA was performed on the thicker sample D (see Experimental Section for details and Table 1) to maximize the signal obtained from XRD and Raman characterizations. ZnS-SiO_2 (≈35 nm) was chosen as a capping since it offers good optical transparency, relatively low stress, and good diffusion blocking. The temperature range considered was 200–450°C, with steps separated by 25°C intervals (only the 225°C step was omitted). Each annealing consists of a fast heat-up ramp of 10 s to the desired temperature, followed by a 30 min hold-temperature step, and finally a cooling down step (with purging). Afterward, the sample was unloaded, and its AFM, XRD, Raman, and PL spectra were measured. The sample was then annealed at a higher temperature, and the ex situ measurements were repeated. In this way, the structure and properties of the sample after a given annealing stage depend on the annealing history. The ω-2θ scans of the as-grown h-GaTe and after each annealing step are reported in Figure 3a. The

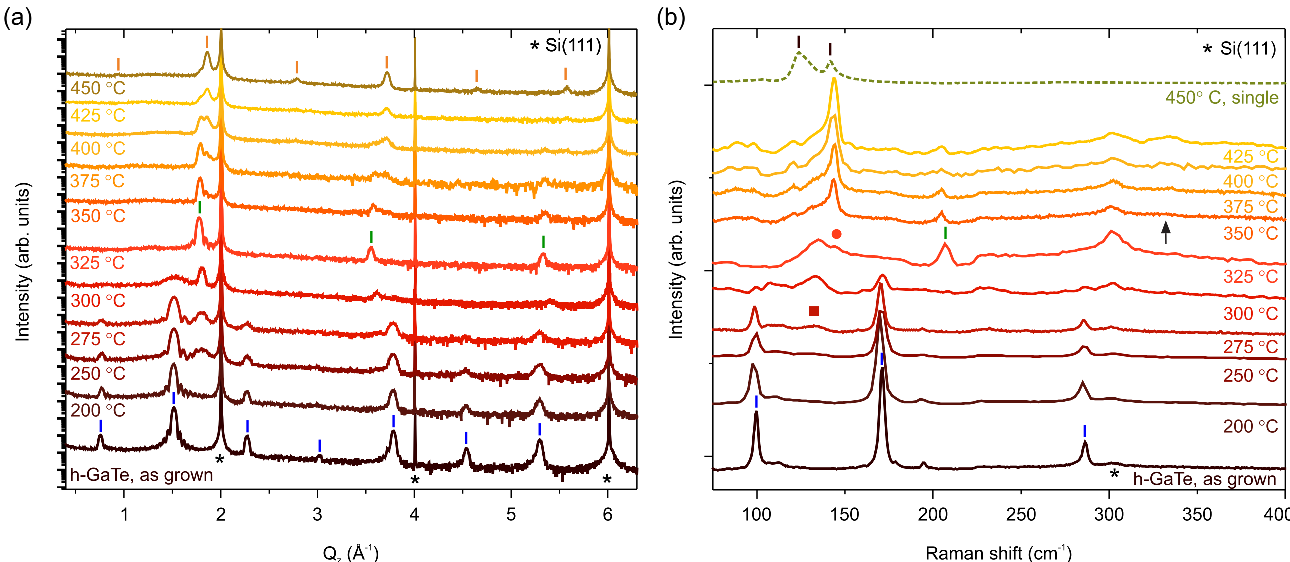

FIGURE 3 | Phase stability of the epitaxial h-GaTe film as a function of rapid thermal annealing (RTA) temperature. (a) and (b) Symmetric out-of-plane ω-2θ scan and Raman spectra excited with a 473 nm laser excitation, respectively, of as-grown h-GaTe (sample D) and after RTA in the range 200–450°C. The XRD scans are presented with a vertical offset to visualize the change in the Bragg diffraction with temperature, and probe exclusively vertical lattice properties of the sample. The vertical axis for the Raman data has been rescaled for clarity. The Raman at 450°C is the result of a single annealing of the as-grown h-GaTe. The vibrational and diffraction modes from h-GaTe, the additional ZnTe phase formation at 325°C, and the final phase transformation at 450°C are highlighted with blue, green, and orange lines, respectively.

18626270, 2026, 2, Downloaded from https://onlinelibrary.wiley.com/doi/10.1002/pssr.202500432 by CochraneItalia, Wiley Online Library on [12/06/2026]. See the Terms and Conditions (https://onlinelibrary.wiley.com/terms-and-conditions) on Wiley Online Library for rules of use; OA articles are governed by the applicable Creative Commons License

Bragg reflections from the pristine sample confirm the out-of-plane stacking of the hexagonal phase [16], as shown by the 002 reflection at $Q_z = 0.769\,\text{Å}^{-1}$ and the others equally spaced by $0.76\,\text{Å}^{-1}$, resulting in an out-of-plane lattice c of 16.610 ± 0.004 Å. Interestingly, h-GaTe grown on non-passivated substrates (samples A and B) manifests the same crystal structure as the growths on passivated ones (sample C) with an average c spacing of 16.629 ± 0.029 Å (see Figure S4, Supporting Information), which is 1.5% larger than the value reported in literature for bulk h-GaTe [9]. This highlights that c is almost strain-free regardless of substrate treatment, as expected for a material grown via vdW epitaxy. In the case of sample D, the smaller values (0.5% and 0.1%, respectively) of the in-plane and out-of-plane lattice constants with respect to the other samples are attributed to the larger incorporation of Ga and Te (see QMS data in Figures 1 and 2), but dedicated studies are needed to shed light on the possible scenarios.

As the annealing temperature increases to 200°C, h-GaTe features persist with no significant intensity change in the spectra apart from a slight broadening of the peaks. The onset of the first transformation is visible at 250°C, where the intensity (full width at half maximum, FWHM) of the diffraction peaks (0 0 2l) from h-GaTe decreases (increases), while a broader peak emerges between 1.7 and $1.8\,\text{Å}^{-1}$. This peak narrows as a function of annealing temperature with the appearance at 300°C of its higher orders (3.6 and $5.4\,\text{Å}^{-1}$). Simultaneously, the intensity of the (0 0 2l) peaks of h-GaTe is strongly suppressed, accompanied by a FWHM broadening as the result of partial amorphization (see further discussion later in the text) until 325°C, where three evenly spaced Bragg reflections at 1.78, 3.56, and $5.33\,\text{Å}^{-1}$ are visible. By using the equation

$$d_{111} = 2\pi/\Delta Q_z \quad (1)$$

which applies to a pseudocubic lattice, a new periodicity of 3.53 Å and a lattice parameter $a = \sqrt{3}d_{111} = 6.1$ Å have been found. By considering the average from the higher orders, we obtain $a = 6.12$ Å, which is well-matched by the zincblend ZnTe of 6.10 Å [25]. The formation of ZnTe oriented along the [111] direction is supported by Raman characterization and tentatively ascribed to the diffusion of some capping material into the epilayer (see further discussion in Section 2.2.2). From 350 up to 425°C, we observe new bumps rising at higher Q_z, which become clear peaks at 375°C while the ZnTe periodicity disappears almost completely at 425°C. The second phase transformation is visible at 450°C with a complete series of Bragg reflections starting at $Q_z = 0.94\,\text{Å}^{-1}$, which corresponds to an interplanar spacing d of 6.69 Å. This value is much smaller than the m-GaTe (7.40 Å) obtained after RTA of the same h-GaTe epitaxial material to higher temperature (550°C) and different capping layer (Si_3N_4) [16], as evidenced by the absence of the fingerprint peak at $1.643\,\text{Å}^{-1}$ for the (−4 2 0) plane [16, 26, 27]. Interestingly, we observed that the tetragonal GaTe phase (T-GaTe) [28] aligns with the peak positions with an error of only 2%. We envision that advanced imaging techniques, such as transmission electron microscopy (TEM), are necessary for a better understanding of the nature of these crystalline structures and to distinguish between intrinsic phase transformation and interface-driven recrystallization. It is important to note that we observed a change in the surface morphology above 325°C with the appearance of hillocks and a rip-off of the capping layer starting from 425°C (see Figure S5, Supporting Information). Even though ZnS-SiO_2 is stable up to 400°C for short thermal pulses [29], the longer annealing time and cumulative thermal budget from repeated lower-temperature RTA runs could explain the progressive deterioration of the capping layer, which enabled Zn/S interdiffusion and the likely formation of an interfacial ZnTe layer at 325°C.

In order to get more insight into the two new structural transformations of the epitaxial layer and additional signatures from the morphological and compositional change of the capping layer, we report in Figure 3b the respective Raman spectra obtained with blue laser excitation. Raman data from the pristine material show three main modes at 100.4, 172.1, and $287.3\,\text{cm}^{-1}$ that are A^1_{1g}, E^1_{2g}, and A^2_{1g} for h-GaTe epilayer, respectively [16]. The feature at $302.6\,\text{cm}^{-1}$ is ascribed to the silicon substrate, whereas two additional bumps are observed at 113.3 and $195.5\,\text{cm}^{-1}$. The weaker intensity of these two modes under red laser excitation (see Figure S6, Supporting Information) may indicate that different phases are forming closer to the interface with the capping layer, due to the larger penetration depth of the source. Neither T_{sub}, $\Phi_{\text{Ga/Te}}$, nor substrate passivation has had any effect on the Raman spectrum with a peak shift for samples A–D that is generally within the error bar (see Figure S4, Supporting Information). Therefore, the equivalent strain value is consistent with the XRD data and serves as another indication of successful vdW epitaxy.

Figure 3b shows a change in the spectrum at 250°C with a new mode appearing at $134\,\text{cm}^{-1}$ (see square) and increasing in intensity at 275°C, which we propose as corresponding to amorphous GaTe, as reported in Ref. [30] after annealings at comparable temperatures (see the discussion on the annealing in situ in Section 2.2.2). Simultaneously, a doublet at $\approx 113\,\text{cm}^{-1}$ emerges. This feature lies very close to intrinsic phonons reported for m-GaTe [16]; however, its pronounced broadening and intensity increase could be the result of disorder-activation or the emergence of localized/amorphous vibrational states. As the temperature increases, the spectrum evolves quite consistently with the XRD data, but the appearance of the ZnTe LO mode at $206.9\,\text{cm}^{-1}$ [31, 32] is visible only at 300°C and becomes more pronounced at 325 up to 425°C. This is a clear indication of the chemical contamination of the buried film from the capping layer, resulting from material diffusion. Interestingly, no signature of the ZnTe LO mode is present when the sample is excited with a red laser (1.96 eV, see Figure S6, Supporting Information). We tentatively attribute this observation to the lower Raman intensity at higher wavelength (λ) based on the λ^{-4} scaling law and to the close to resonant enhancement of this mode with the blue laser (2.62 eV) since the bandgap at RT of ZnTe is 2.26 eV [33]. Different from XRD, at 325°C, another Raman mode starts emerging at $144.5\,\text{cm}^{-1}$ (see the circle in Figure 3b) and becomes sharp at 350°C with the mode at $134\,\text{cm}^{-1}$ still visible as a shoulder. The increase in the intensity of the $144.5\,\text{cm}^{-1}$ mode as a function of temperature can be the result of Te segregation followed by GaTe decomposition and oxidation [34] due to the instability of the capping layer (see Figure S5, Supporting Information). Furthermore, the pronounced mode at higher temperatures and its nearly stable energy position suggest that oxidation is localized closer to the surface after

18626270, 2026, 2, Downloaded from https://onlinelibrary.wiley.com/doi/10.1002/pssr.202500432 by CochraneItalia, Wiley Online Library on [12/06/2026]. See the Terms and Conditions (https://onlinelibrary.wiley.com/terms-and-conditions) on Wiley Online Library for rules of use; OA articles are governed by the applicable Creative Commons License

material segregation. It is important to note that it was not possible to measure a Raman spectrum at 450°C due to the very poor quality of the sample surface. For this reason, we annealed the as-grown h-GaTe directly to the final temperature, and observed an XRD spectrum (not shown) similar to the one reported in Figure 3a. The Raman spectrum shows two modes at 124 and 142 cm^{-1}. These are consistent with the A_1 and E modes of trigonal Te after the decomposition and oxidation of GaTe when exposed to air [34]. However, to date, investigations have primarily addressed m-GaTe, leaving the oxidation processes of pristine h-GaTe largely uncharacterized.

2.2.2 | In Situ Raman During Annealing

To follow the transition from crystalline h-GaTe to the loss of long-range order via the formation of amorphous GaTe and to confirm that the approach used for the RTA series is consistent and reliable, we carried out Raman spectroscopy measurements as a function of annealing by using a hot plate (see Experimental Section) by increasing the temperature in smaller step sizes, as shown in Figure 4. For this experiment, we used sample C, which was grown at a lower growth rate compared to sample D, resulting in a thinner film (see Table 1). Accordingly, the Raman spectrum at RT is consistent with the h-GaTe phase (see Section 2.2.1 and Ref. [16]). At 225°C a bump emerges at 117 cm^{-1} and its intensity increases up to 300°C, as shown also for sample D. When the h-GaTe modes are strongly weakened (250°C), another broader mode at 130 cm^{-1} becomes more pronounced (see the square in Figure 4). This is consistent with the amorphization of the GaTe crystal observed in sample D, and it is assigned, following Bokova et al. [30], to Te–Te vibrations in GaTe glasses with more pronounced Ga_2Te_3 composition (α-GaTe(1)). As the temperature increases to 300°C, another bump rises at around 162 cm^{-1} (see the triangle in Figure 4), which is very close to the other GaTe-related vibrations in GaTe glasses reported by Ref. [30] (α-GaTe(2)). Similar to sample D, at higher temperature (345°C), an additional peak at 144.4 cm^{-1} starts appearing (see the circle in Figure 4), which is related to Te segregation followed by the oxidation of GaTe due to the already described poor passivation of the epitaxial film. The observed Raman spectrum may originate from local structural rearrangements rather than a wholesale transformation into a different phase, as demonstrated in the work by Zhou et al. [35].

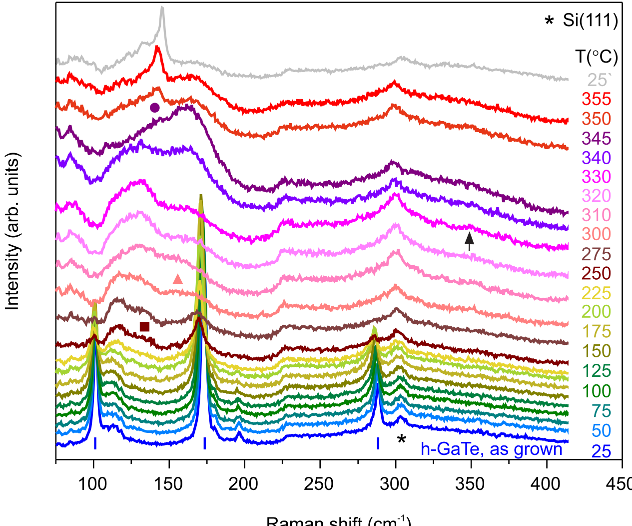

FIGURE 4 | Phase stability of the epitaxial h-GaTe films during annealing in situ via hot plate. Temperature-dependent Raman spectra of the as-grown h-GaTe (sample C, blue lines) recorded from room temperature (RT) up to 355°C with a 473 nm laser excitation. The amorphous peaks α-GaTe(1) and α-GaTe(2) are indicated by a square and a triangle, respectively, whereas the circle and arrow indicate the position of the Te and the ZnS-like LO modes, respectively. The final Raman spectrum at 25°C with prime labeling (gray) was measured after cooling down the sample to RT at the end of the series and has been scaled for clarity.

A careful screening of the Raman spectra in Figure 4 evidences the role of material diffusion and chemical contamination of the buried film. In particular, a bump in the energy range 340–350 cm^{-1} appears already at 250°C and gets more pronounced at higher temperatures with a clear signature at 330°C (see arrow), where no products of Te segregation can be detected yet. In the case of RTA we observed an analogous mode in the same energy range (335 cm^{-1}) at much higher temperatures (350°C, see Figure 3b), which we tentatively attribute to ZnS-like LO mode for zinc blend ZnS at RT. In addition, the intensity of this mode increases, whereas the ZnTe-like one is suppressed as the temperature rises. In fact, Raman studies of ZnS_xTe_{1-x} alloys demonstrate the coexistence of ZnTe and ZnS phonon modes, with a gradual transfer of intensity from the ZnTe-like LO ($\approx$210 cm^{-1}) to the ZnS-like LO ($\approx$340–350 cm^{-1}) as the sulfur content increases [36]. The frequency shift of this Raman peak could be used to probe the composition of the ZnS_xTe_{1-x} material after diffusion from the capping layer. It is important to note that the ZnTe mode is not clearly visible in the sample annealed in situ with a hot plate (sample C). However, XRD spectra at 330 and 355°C (see Figure S7, Supporting Information) show a pseudocubic (111)-oriented pattern. By using the Vegard's law $a(x) \sim x a_{ZnS} + (1-x) a_{ZnTe}$ (see Ref. [32] for the lattice parameters of ZnS and ZnTe), we estimate a lattice parameter $a \approx 5.94$ Å matching a ZnS_xTe_{1-x} alloy with $x = 0.23$, which is the result of interdiffusion from the ZnS-SiO_2 capping layer [37]. Finally, we propose that rapid thermal cycles by RTA favor near-surface transformation by nucleating Te-rich ZnTe islands or forming a thin ZnTe-rich surface layer, which lies within the Raman sampling depth. In the case of annealing via standard hot plate and slower ramps, Zn and S diffuse more uniformly into the chalcogenide layer [38]. Characterization techniques such as X-ray photoemission spectroscopy (XPS) and cross-sectional TEM are envisioned to confirm interfacial oxidation and to map the depth and morphological distribution of the different species.

From the experimental results obtained, we can conclude that it is possible to alter the crystal structure of h-GaTe by annealing, as evidenced by the changes in both Raman and XRD spectra with increasing temperature. Furthermore, the stability of the capping layer varies depending on the thermal treatment applied.

2.2.3 | Optical Activity

To figure out the optical activity of the annealed samples and develop a clearer picture of the new observed phases, we measured PL for as-grown h-GaTe (sample D, see Table 1) and after RTA at 325, 425, and 450°C. As shown in Figure 5, the as-grown h-GaTe evidences no PL emission, as expected for the hexagonal phase [16]. At the annealing temperature of 325°C, a weak band

18626270, 2026, 2, Downloaded from https://onlinelibrary.wiley.com/doi/10.1002/pssr.202500432 by CochraneItalia, Wiley Online Library on [12/06/2026]. See the Terms and Conditions (https://onlinelibrary.wiley.com/terms-and-conditions) on Wiley Online Library for rules of use; OA articles are governed by the applicable Creative Commons License

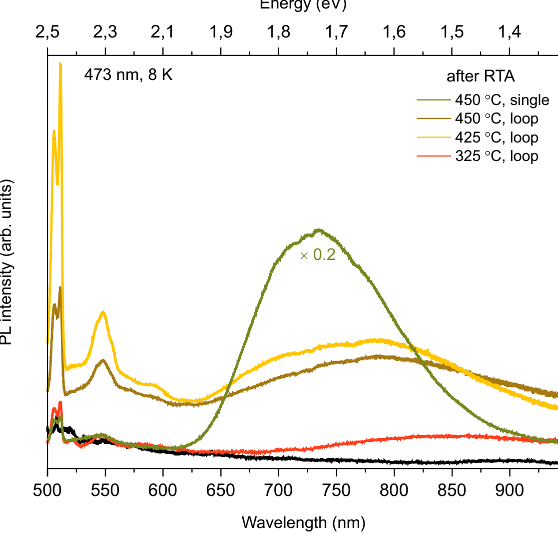

FIGURE 5 | Optical activity of epitaxial h-GaTe after RTA. Low-temperature photoluminescence spectra at 8 K and 473 nm laser excitation from as-grown h-GaTe (sample D, black) and after RTA at 325 (red), 425 (yellow), and 450°C (brown and green). The labels "single" and "loop" represent a single or iterative annealing step before the measurement.

appears above 700 nm, which is provisionally attributed to defect/oxide states, but further structural and chemical analysis is required.

At 425°C, the optical response changes dramatically with the appearance of a PL band centered at around 750 nm (≈1.65 eV), which is also visible at 450°C (see brown spectrum). The PL peak center is very close to the one reported by our group from the m-GaTe annealed at higher temperatures (550°C) and using a Si_3N_4 capping layer [16]. However, XRD and Raman data do not match with the m-GaTe crystal phase but could be the transition to the intermediate metastable T-GaTe predicted by Zhao et al. [39] (see previous discussion of Figure 3). Nevertheless, the observed PL energy cannot be explained by the presence of T-GaTe [40]. Instead, the emission may arise from GaTe-related subgap states or from incipient monoclinic-like domains, although further studies are required to discriminate between these possibilities. It is important to note that the sample after RTA at 450°C with only one ramp (see green spectrum) shows a much stronger PL signal than the one from the sample annealed at the same temperature with repeated cycles. This highlights the critical role of a more stable passivation layer. However, the damage of the capping layer seems not to be affecting the epitaxial layer at least up to 350°C (see Figure S5, Supporting Information), as confirmed by the same GaTe Raman features measured after RTA and in situ annealing via hot plate.

Interestingly, by looking at the PL spectrum in the high-energy region, we observe a doublet at 506–511 nm (≈2.43–2.45 eV) and a broader peak at 550 nm (≈2.25 eV), which emerges at 325°C and increases in intensity with the annealing temperatures, having a maximum at 425°C. The high-energy features can be attributed to ZnTe-like domains or ZnS_xTe_{1-x} near-surface regions. In fact, pure ZnTe exhibits a low-temperature bandgap of ≈2.36–2.40 eV, and previous optical studies have shown that alloying with sulfur, as well as strain or size confinement, can blueshift the excitonic emission into the 2.4–2.5 eV range [41]. The 550 nm (2.25 eV) peak is below the typical ZnTe exciton, compatible with defect-bound emission, donor–acceptor lines, or a slightly Te-richer phase [42]. The coexistence of sharp PL peaks with surface-sensitive Raman signatures assigned to Zn(S)- and Te-related modes (see the spectrum at 425°C in Figure 3b), together with the absence of distinct ZnTe reflections in conventional XRD spectrum (see Figure 3a), is consistent with a low-volume, near-surface population of small or strained Zn(Te,S) domains below the XRD detection limit. To further validate this scenario, complementary analyses such as GID-XRD, XPS depth profiling, and cross-sectional TEM at locations identified by spatial PL/Raman mapping would be necessary.

3 | Conclusion

In conclusion, we investigated the influence of substrate temperature, Ga/Te flux ratio, and substrate passivation on the large-area epitaxial growth of h-GaTe on Si(111). A comprehensive analysis combining structural, morphological, and spectroscopical characterizations reveals that the growth rate is primarily governed by Ga flux, while Te must be supplied in excess due to its high volatility. Lower substrate temperatures enhance the growth rate, and Sb passivation modifies nucleation dynamics without significantly affecting the final morphology. Across all samples, the in-plane lattice spacing relaxes to 4.112 ± 0.012 Å, with one or two oscillations during the first four layers, followed by a gradual increase of 0.2–0.6% for thicker films. The 2D to 3D transition is observed after lattice relaxation and is attributed to changes in wetting conditions rather than strain release. Annealing experiments reveal that as-grown h-GaTe undergoes amorphization around 250°C, followed by transformation into an optically active phase at ≈450°C. Raman and XRD further highlight the instability of the ZnS-SiO_2 capping layer at ≈350°C, where elemental diffusion leads to Zn(S)Te alloy formation within the GaTe layer and its partial oxidation. Overall, these findings provide new insights into the interplay of growth kinetics, wetting, and phase stability in metastable layered materials, and point to future work needed to clarify the microscopical mechanisms underlying the observed phase transformations.

4 | Experimental Section

4.1 | MBE

The GaTe films were grown by solid-source MBE on Si(111) with 0.03° miscut. After standard silicon cleaning, the Si(111)-(7 × 7) reconstruction was obtained by heating up the substrates to 720°C at a rate of 0.2°C for 5 min. In the case of Sb passivation, the surfaces were exposed to a Sb flux for 5 min and cooled down to 650°C at a rate of 0.3°C. After an additional 5 min, the temperature is cooled down to 300°C at the same rate and annealed for 3 min before the Sb shutter was closed and the Si(111)-($\sqrt{3} \times \sqrt{3}$)R30° appeared on the RHEED screen.

4.2 | QMS

The QMS (Hiden HAL 511 PIC) comprises a Pirani–ionization combination (PIC) gauge, fitted with a standard UHV low-profile source, and is installed in a dedicated port of the MBE chamber

18626270, 2026, 2, Downloaded from https://onlinelibrary.wiley.com/doi/10.1002/pssr.202500432 by CochraneItalia, Wiley Online Library on [12/06/2026]. See the Terms and Conditions (https://onlinelibrary.wiley.com/terms-and-conditions) on Wiley Online Library for rules of use; OA articles are governed by the applicable Creative Commons License

for line-of-sight measurements. An aperture was placed between the substrate and the ionization grid to reduce the line-of-sight acceptance angle of the detector to exclude atoms that do not originate on the wafer surface. A mechanical shutter is used to distinguish between the background signal and the actual signal from the ion beam.

4.3 | AFM

Tapping mode AFM (Veeco Nanoscope III) was employed to probe the surface morphology.

4.4 | XRD

Samples were characterized by means of ex situ XRD, utilizing specular ω-2θ scans in double axes mode in order to probe lattice properties along growth direction with a 1 mm slit at the detector side. The lattice properties within the GaTe layers were probed by GID experiments at the PHARAO beamline at the U125/2-KMC (BESSYII, Helmholtz–Zentrum Berlin) using an X-ray energy of 12 keV. The layer thicknesses were also estimated by XRR (see Figure S8, Supporting Information).

4.5 | Raman Spectroscopy

Micro-Raman measurements were conducted in backscattering geometry using a Horiba LabRAM Evolution 800 mm Spectrograph with 473 and 632.8 nm continuous wave laser excitations at RT (1 µm diameter spot). The character of the vibrational modes was assigned using polarization-resolved spectroscopy. For the temperature-dependent Raman scattering measurements, a heating stage Linkam was used in the temperature range of 300–630 K.

4.6 | PL Spectroscopy

PL measurements were carried out using a liquid-He flow cryostat at 8 K with 473 nm laser focused to a diameter of 1 µm.

4.7 | RTA

The phase transformation of the as-grown h-GaTe was studied in a RTA furnace JetFirst 100 under 1 bar nitrogen atmosphere in the temperature range 200–450°C for 30 min. The sample is placed on a Si wafer in the chamber and heated by halogen bulbs fixed on the top of the chamber under an N_2 environment. The annealing (cooling) ramp rate was 40°C/s (1°C/s). The sample temperature is controlled by a thermocouple in direct contact with the wafer. The annealing time has been chosen to allow the sample structure to reach thermodynamic equilibrium.

Acknowledgments

The authors would like to thank M. Ramsteiner, M. Bissolo for fruitful discussions, C. Stemmler, C. Hermann, and M. Höricke for their dedicated maintenance of the MBE and RTA systems, and MIET Moscow for the support with the electron microscopy studies. The work was partly funded by the German Research Foundation (DFG) via Grants FI 947/7-1, FI 947/8-1 and KO4005-9/1, and by the European Union's Horizon 2020 research and innovation program under Grant Agreement No. 824957 ("BeforeHand": Boosting Performance of Phase Change Devices by Hetero- and Nanostructure Material Design).

Open Access funding enabled and organized by Projekt DEAL.

Funding

This study was supported by HORIZON EUROPE European Innovation Council (Grant 824957), and Deutsche Forschungsgemeinschaft (Grant FI 947/7-1, FI 947/8-1, and KO4005-9/1),

Conflicts of Interest

The authors declare no conflicts of interest.

Data Availability Statement

The data that support the findings of this study are available from the corresponding author upon reasonable request.

References

1. H. Cai, Y. Gu, Y.-C. Lin, Y. Yu, D. B. Geohegan, and K. Xiao, "Synthesis and Emerging Properties of 2D Layered III–VI Metal Chalcogenides," *Applied Physics Reviews* 6, no. 4 (2019): 041312.

2. Y. Fu, Z. Liu, S. Yue, K. Zhang, R. Wang, and Z. Zhang, "Optical Second Harmonic Generation of Low-dimensional Semiconductor Materials," *Nanomaterials* 14, no 8 (2024): 662.

3. C. Rocha Leão and V. Lordi, "Ab Initio Guided Optimization of GaTe for Radiation Detection Applications," *Physical Review B* 84 (2011): 16.

4. F. Liu, H. Shimotani, H. Shang, et al., "High-sensitivity Photodetectors Based on Multilayer GaTe Flakes," *ACS Nano* 8 (2014): 1–752.

5. C. C. Sta Maria, P.-H. Wu, D. P. Hasibuan, et al., "Efficient Van Der Waals Layered Gallium Telluride-Based Passive Photodetectors for Low-Power-Density Sensing of Visible Light," *Journal of Materials Chemistry C* 11, no. 41 (2023): 14316–14325.

6. T. Singha, M. Karmakar, P. Kumbhakar, C. S. Tiwary, and P. K. Datta, "Atomically Thin Gallium Telluride Nanosheets: A New 2D Material for Efficient Broadband Nonlinear Optical Devices," *Applied Physics Letters* 120 (2022): 2.

7. B. Marfoua and J. Hong, "High Thermoelectric Performance in Two Dimensional Chalcogenides Systems: GaSe and GaTe," *Nanotechnology* 32 (2021): 11–115702.

8. T. Cao, Z. Li, and S. G. Louie, "Tunable Magnetism and Half-Metallicity in Hole-Doped Monolayer GaSe," *Physical Review Letters* 114, no: 23 (2015): 236602.

9. E. G. Gillan and A. R. Barron, "Chemical Vapor Deposition of Hexagonal Gallium Selenide and Telluride Films from Cubane Precursors," *Chemistry of Materials* 9, no. 12 (1997): 3037.

10. Y. Gutiérrez, S. Dicorato, E. Dilonardo, F. Palumbo, M. M. Giangregorio, and M. Losurdo, "Stability of Nanometer-Thick Layered Gallium Chalcogenides and Improvements Via Hydrogen Passivation," *ACS Applied Nano Materials* 6, no. 21 (2023): 20161–20172.

11. C. H. Lee, S. Krishnamoorthy, D. J. O'Hara, et al., "Molecular Beam Epitaxy of 2D-Layered Gallium Selenide on GaN Substrates," *Journal of Applied Physics* 121 (2017): 9–094302.

12. M. Bissolo, M. Dembecki, J. Belz, et al., "Unveiling the Growth Mode Diagram of GaSe on Sapphire," *Communications Materials*, 6, no. 1 (2025): 279, https://arxiv.org/abs/2510.10743.

18626270, 2026, 2, Downloaded from https://onlinelibrary.wiley.com/doi/10.1002/pssr.202500432 by CochraneItalia, Wiley Online Library on [12/06/2026]. See the Terms and Conditions (https://onlinelibrary.wiley.com/terms-and-conditions) on Wiley Online Library for rules of use; OA articles are governed by the applicable Creative Commons License

13. M. S. Claro, J. Grzonka, N. Nicoara, P. J. Ferreira, and S. Sadewasser, “Wafer-Scale Fabrication of 2D β-In_2Se_3 Photodetectors,” *Advanced Optical Materials* 9, no. 1 (2021): 2001034.

14. M. Hilse, J. Rodriguez, J. Gray, et al., “Mixed Polytype/Polymorph Formation in InSe Films Grown by Molecular Beam Epitaxy on GaAs(111)B,” *npj 2D Materials and Applications* 9, no. 1 (2025): 19.

15. Q. T. Tran, T. B. T. Huynh, T. H. Pham, et al., “Molecular Beam Epitaxy of Mixed Dimensional InGaSe/GaSe Hybrid Heterostructures on c-Sapphire,” *ACS Applied Electronic Materials* 6, no. 10 (2024): 7448–7455.

16. E. Zallo, A. Pianetti, A. S. Prikhodko, et al., “Two-Dimensional Single Crystal Monoclinic Gallium Telluride on Silicon Substrate Via Transformation of Epitaxial Hexagonal Phase,” *npj 2D Materials and Applications* 7, no. 1 (2023): 19.

17. W. Quan, X. Wu, Y. Cheng, et al., “Phase Modulation of 2D Semiconducting GaTe from Hexagonal to Monoclinic through Layer Thickness Control and Strain Engineering,” *Nano Letters* 25, no. 16 (2025): 6614–6621.

18. M. Bissolo, M. Hanke, R. Calarco, et al., “Van Der Waals Epitaxy of 2D Gallium Telluride on Graphene: Growth Dynamics and Principal Component Analysis,” *Small* 21 (2025): 24.

19. J. E. Boschker, J. Momand, V. Bragaglia, et al., “Surface Reconstruction-Induced Coincidence Lattice Formation Between Two-Dimensionally Bonded Materials and a Three-Dimensionally Bonded Substrate,” *Nano Letters* 14, no. 6 (2014): 3534.

20. D. S. H. Liu, M. Hilse, and R. Engel-Herbert, “Sticking Coefficients of Selenium and Tellurium,” *Journal of Vacuum Science & Technology A: Vacuum Surfaces, and Films* 39, no. 2 (2021): 023413.

21. S. Cecchi, T. Etzelstorfer, E. Müller, et al., “Ge/SiGe Superlattices for Thermoelectric Energy Conversion Devices,” *Journal of Materials Science* 48, no. 7 (2012): 2829–2835.

22. J. Massies and N. Grandjean, “Oscillation of the Lattice Relaxation in Layer-By-Layer Epitaxial Growth of Highly Strained Materials,” *Physical Review Letters* 71, no. 9 (1993): 1411–1414.

23. J. D. Fuhr and P. Müller, “Physical Origin of In-Plane Lattice Spacing Oscillations Measured by Reflection High-Energy Electron Diffraction During Epitaxial Growth,” *Physical Review B* 84 (2011): 19.

24. E. Zallo, D. Dragoni, Y. Zaytseva, et al., “Evolution of Low-Frequency Vibrational Modes in Ultrathin GeSbTe Films,” *Physica Status Solidi (RRL) – Rapid Research Letters* 15 (2020): 3.

25. P. Paufler, “Landolt-Börnstein. Numerical Data and Functional Relationships in Science and Technology - New Series, Group III: Crystal and Solid State Physics, vol. 22: Semiconductors. Subvolume a: Intrinsic Properties of Group IV Elements and III-V, II-VI and I-VII Compounds,” *Crystal Research and Technology* 23, no. 10–11 (1988): 1360-1360.

26. X. Yuan, L. Tang, P. Wang, et al., “Wafer-Scale Arrayed p-n Junctions Based on Few-Layer Epitaxial GaTe,” *Nano Research* 8, no. 10 (2015): 3332.

27. C. J. Bae, J. McMahon, H. Detz, et al., “Influence of Thickness on Crystallinity in Wafer-Scale GaTe Nanolayers Grown by Molecular Beam Epitaxy,” *AIP Advances* 7, no. 3 (2017): 035113.

28. M. Julien-Pouzol, S. Jaulmes, and F. Alapini, “Monotellurure De Gallium, GaTe,” *Acta Crystallographica Section B Structural Crystallography and Crystal Chemistry* 33, no. 7 (1977): 2270–2272.

29. D. V. Tsu and T. Ohta, “Mechanism of Properties of Noble ZnS–SiO_2 Protection Layer for Phase Change Optical disk Media,” *Japanese Journal of Applied Physics* 45, no. 8R (2006): 6294.

30. M. Bokova, A. Tverjanovich, C. J. Benmore, et al., “Unraveling the Atomic Structure of Bulk Binary Ga–Te Glasses with Surprising Nanotectonic Features for Phase-Change Memory Applications,” *ACS Applied Materials & Interfaces* 13, no. 31 (2021): 37363–37379.

31. E. M. Larramendi, G. Berth, V. Wiedemeier, et al., “Intensity Enhancement of Te Raman Modes by Laser Damage in ZnTe Epilayers.32- Raman Scattering Study of Zinc Blende and Wurtzite ZnS,” *Semiconductor Science and Technology* 25, no. 7 (2010): 075003.

32. Y. C. Cheng, C. Q. Jin, F. Gao, et al., “Raman Scattering Study of Zinc Blende and Wurtzite ZnS,” *Journal of Applied Physics* 106 (2009): 12.

33. S. Adachi, Optical Constants of Crystalline and Amorphous Semiconductors (Springer US, 1999), 473–486. ISBN. 9781461552475.

34. F. J. Manjón, S. Gallego-Parra, P. Rodríguez-Hernández, et al., “Anomalous Raman Modes in Tellurides,” *Journal of Materials Chemistry C* 9, no. 19 (2021): 6277–6289.

35. Y. Zhou, S. Zhou, P. Ying, et al., “Unusual Deformation and Fracture in Gallium Telluride Multilayers,” *The Journal of Physical Chemistry Letters* 13, no. 17 (2022): 3831–3839.

36. C. X. Jin, Z. Ling, D. H. Wang, D. M. Huang, X. Y. Hou, and X. Wang, “Phonon Modes of $ZnS_{1-x}Te_x$ Alloys Epitaxially Grown on (100) GaAs Substrates,” *Journal of Applied Physics* 81, no. 8 (1997): 3465–3467.

37. S. Cecchi, I. L. Garcia, A. M. Mio, et al., “Crystallization and Electrical Properties of Ge-Rich GeSbTe Alloys,” *Nanomaterials* 12, no. 4 (2022): 631.

38. T. Müller, M. Gehmlich, A. Sattler, et al., “Near-Surface Defect Control by Vacancy Injecting/Out-Diffusing Rapid Thermal Annealing,” *Physica Status Solidi (a)* 216 (2019): 17.

39. Q. Zhao, T. Wang, Y. Miao, et al., “Thickness-Induced Structural Phase Transformation of Layered Gallium Telluride,” *Physical Chemistry Chemical Physics* 18 (2016): 28–18719.

40. A. Tverjanovich, C. J. Benmore, M. Khomenko, et al., “Decoding The Atomic Structure of Ga_2Te_5 Pulsed Laser Deposition Films for Memory Applications Using Diffraction and First-Principles Simulations,” *Nanomaterials* 13, no. 14 (2023): 2137.

41. K. Yoshino, A. Memon, M. Yoneta, K. Ohmori, H. Saito, and M. Ohishi, “Optical Characterization of The ZnTe Pure-Green LED,” *Physica Status Solidi (b)* 229, no. 2 (2002): 977–980.

42. H. Venghaus and P. J. Dean “Shallow-Acceptor, Donor, Free-Exciton, and Bound-Exciton States in High-Purity Zinc Telluride,” *Physical Review B* 21, no. 4 (1980): 1596–1609.

Supporting Information

Additional supporting information can be found online in the Supporting Information Section. **Supporting Fig. S1:** Reflection high-energy electron diffraction (RHEED) oscillations. (a-c) RHEED oscillations for samples A, B, and C for full growth time (80 min). The 2D-3D transition, marked by the formation of a spotty pattern, is indicated by the dotted line. The dashed line at the beginning of the growth of sample C is a plausible reconstruction of the first missing minutes, based mainly on the length of the following oscillations and partially considering the trends observed in other samples. **Supporting Fig. S2:** Transmission electron microscopy of the interface region for sample C. (left) The HRTEM image of the interface between Si and h-GaTe epilayer illustrates the transition between the crystalline substrate and the 2D epilayer through the Sb/Ga bilayer. (right) The HAADF STEM image highlights the presence of heavy atoms, such as Sb, in the transition Sb/Ga bilayer. **Supporting Fig. S3:** In-plane mosaicity. (a) In-plane section as probed by grazing incidence diffraction for as-grown sample C. The coordinates are given in reciprocal lattice units (rlu). Besides the substrate reflections, there are pronounced layer peaks connected by a dotted arc. Such azimuthal scans are shown in (b) for two as-grown h-GaTe (samples B and C). Similar domains are also observed at 30° and 60° for sample D. **Supporting Fig. S4:** Effect of growth parameters. (a) Symmetric out-of-plane ω-2θ scan and (b) Raman spectra with a 473 nm laser excitation from as-grown h-GaTe (samples A-D). The X-ray diffraction (XRD) scans probe the vertical lattice properties of the sample exclusively. **Supporting Fig. S5:** Surface topography as a function of annealing temperature. Atomic force microscopy height image of the h-GaTe (sample

18626270, 2026, 2, Downloaded from https://onlinelibrary.wiley.com/doi/10.1002/pssr.202500432 by CochraneItalia, Wiley Online Library on [12/06/2026]. See the Terms and Conditions (https://onlinelibrary.wiley.com/terms-and-conditions) on Wiley Online Library for rules of use; OA articles are governed by the applicable Creative Commons License

D) after RTA at (a) 200, (b) 325, (c) 350, and (d) 425°C. Scale bar is 2 μm. **Supporting Fig. S6:** Phase stability as a function of RTA temperature. Raman spectra of as-grown h-GaTe (sample D) and after RTA in the range 200–450°C with a 632.8 nm laser excitation. **Supporting Fig. S7:** Phase transformation during annealing in situ via hot plate. Symmetric out-of-plane ω-2θ scan of as-grown h-GaTe (sample C) and after annealing in situ at 330 and 355°C. **Supporting Fig. S8:** Thickness analysis from X-ray reflectivity (XRR) measurements. (a-d) XRR scans for samples A–D (as-grown h-GaTe), respectively, with the superimposed fit to the data. **Supporting Table S1:** Thickness analysis. Film thickness for the h-GaTe samples A–D as obtained via XRD fringes, XRR fitting, and the period of RHEED oscillations. The estimate for sample D is obtained by averaging the lattice period oscillation, as the RHEED oscillations were not detected.

18626270, 2026, 2, Downloaded from https://onlinelibrary.wiley.com/doi/10.1002/pssr.202500432 by CochraneItalia, Wiley Online Library on [12/06/2026]. See the Terms and Conditions (https://onlinelibrary.wiley.com/terms-and-conditions) on Wiley Online Library for rules of use; OA articles are governed by the applicable Creative Commons License